Reviews of Electromagnetics, Vol. V, 2026
EuCAP 2026 Special Issue
DOI: 10.53792/RoE/2026/26015

Reviews of Electromagnetics
EuCAP 2026 Special Issue

A Dual-Band Millimeter-Wave TT&C Choke-Ring Antenna Developed Using Generative Artificial Intelligence

Nelson J. G. Fonseca[1]*, Charalampos Stoumpos[1], Maddy Clements[2], Alberto Montemiglio[2], Jonathan Davis[2], Tomas Navarro Reverte[3], Nicolas Capet[1]

Abstract
This work explores the use of artificial intelligence (AI) for the design and optimization of millimeter-wave SatCom antennas. The case study reported here is a dual-band choke-ring antenna, a type of antenna that is being considered for future Low Earth Orbit (LEO) satellite constellations, specifically for the Telemetry, Tracking and Command (TT&C) onboard sub-system. The goal of the study was to evaluate the capability of generative AI (GenAI) techniques to improve upon previous results obtained using conventional optimization techniques.
The targeted TT&C application requires a wide beam in two separate bands, with a ratio of approximately 1:1.5. Choke-ring antennas are by design narrow-band and have a high number of design variables, constituting a challenging case for any optimization technique. Despite the limited training data set generated within the study, some improvement in performance has been achieved using a dedicated GenAI tool based on a Variational Autoencoder (VAE).
The best AI-generated antenna profile was selected for verification through the manufacture and test of a fully-functional prototype. A good agreement between numerical and experimental results was achieved. The results reported here showcase the potential of GenAI techniques for the optimization of novel antennas with complex and unconventional profiles. Further studies are required to confirm the conclusions of the work, extending the training dataset with more complex geometries, now within reach thanks to emerging additive manufacturing techniques, and with a more integrated and iterative design process.

Key terms
Artificial intelligence; Choke-ring antenna; Millimeter-wave; Small satellite; Telemetry, Tracking and Command; Variational autoencoder

[1] *Anywaves, Toulouse, France*
[2] *Applied Data Science Partners, London, United Kingdom*
[3] *European Space Agency, Harwell, United Kingdom*
*__Corresponding author__: n.fonseca@anywaves.com

Received: 30/06/2026, Accepted: 02/10/2026, Published: 12/11/2026

1. Introduction

The rapid evolution of satellite communications (SatCom) and next-generation wireless infrastructures, including 5G, 6G, and non-terrestrial networks (NTNs), is creating unprecedented challenges for antenna engineering. Future communication systems require antennas that simultaneously achieve high performance, adaptability, compactness, and efficient integration within increasingly complex and dynamic operating environments [1, 2, 3]. However, conventional antenna design approaches — typically relying on expert-driven intuition, parametric optimization strategies, and computationally intensive electromagnetic (EM) simulations — struggle to efficiently navigate the vast, multidimensional, and highly non-linear design spaces associated with modern antenna architectures. As these traditional methodologies approach their practical scalability limits, artificial intelligence (AI), and particularly generative design techniques, are emerging as transformative tools for antenna synthesis and optimization. By enabling automated

exploration of unconventional geometries, accelerating design iterations, and uncovering high-performing solutions beyond human intuition, AI-driven methods have the potential to significantly enhance innovation, reduce development time, and improve the overall efficiency of advanced antenna design workflows [4, 5, 6, 7].

Generative artificial intelligence (GenAI) introduces a paradigm shift in antenna engineering by moving beyond the optimization of predefined structures toward the autonomous creation of entirely new antenna geometries [8, 9]. Through data-driven learning, these models capture complex relationships between geometrical features, material properties, and electromagnetic performance indicators, enabling the synthesis of innovative designs that satisfy multiple and often conflicting requirements. Compared with conventional optimization techniques, generative approaches can explore large, highly non-linear design spaces more efficiently and uncover unconventional yet high-performing antenna configurations that may remain inaccessible through human intuition alone. When integrated with EM solvers, surrogate modeling, and physics-informed learning strategies, GenAI has the potential to accelerate design cycles, automate early-stage concept generation, and reduce computational costs. These capabilities are particularly valuable for SatCom and next-generation wireless systems, where stringent constraints on size, mass, efficiency, bandwidth, and radiation performance require advanced multi-objective optimization strategies. Furthermore, the rapid growth of computational resources, AI hardware, and accessible open-source machine learning frameworks is further driving the adoption of generative design methodologies across the antenna and radio frequency (RF) engineering community.

The incorporation of generative design methodologies into antenna engineering is opening new perspectives for accelerating and transforming the overall design process. By enabling automated exploration of complex design spaces, GenAI can substantially reduce development times, streamline early-stage concept generation, and enhance the creative capabilities of human designers through the discovery of unconventional yet efficient antenna architectures. When coupled with EM simulation tools, surrogate models, and physics-informed learning techniques, these approaches facilitate the generation of solutions that are not only highly optimized in terms of performance, but also compliant with physical and manufacturing constraints. In addition, the continuous increase in available computational power, together with the widespread accessibility of open-source AI frameworks and high-performance computing resources, is accelerating the transition of generative design from a research topic to a practical engineering tool. As a result, the adoption of AI-driven antenna synthesis methods is rapidly expanding across both academic research and industrial development activities.

In this context, the European Space Agency initiated an Advanced Research in Telecommunications Systems (ARTES) Future Preparation activity dedicated to investigating the application of GenAI to the design and optimization of SatCom systems, with a particular focus on antenna equipment. This initiative reflects the growing interest in leveraging AI-driven methodologies to address the increasing complexity and performance requirements of next-generation space infrastructures. In parallel, new antenna solutions are emerging to support Telemetry, Tracking and Command (TT&C) functionalities in large constellations of small satellites operating in low Earth orbit (LEO) [10]. These developments are associated to the adoption of new frequencies for such purposes, especially within the Ka-band, where larger bandwidths enable enhanced communication links but also introduce significant challenges in terms of antenna efficiency, compactness, beam shaping, and integration constraints. Choke-ring antennas are well known for their capability to produce sectoral patterns, suitable for hemispherical or isoflux coverage [11, 12, 13]. The synthesis is a frequency-dependent process, as the pattern shaping is directly associated to the depth of the chokes (i.e. the concentric metallic grooves around the central radiating waveguide) [14]. Anywaves has conducted studies on the feasibility of dual-band designs, where the transmit (Tx) and receive (Rx) bands are integrated on the same equipment [15, 16]. These antenna architectures were identified as particularly suitable candidates for AI-driven design methodologies owing to their relatively simple geometrical structures, which provide an effective foundation for data-driven optimization and generative exploration. When combined with emerging manufacturing technologies and advanced fabrication techniques, such as additive manufacturing and rapid prototyping, these antenna concepts offer significant potential for the development of innovative solutions [17, 18]. The synergy between GenAI and modern manufacturing capabilities may therefore enable the creation of highly optimized antenna designs that simultaneously address performance, integration, cost, and scalability requirements for future SatCom applications.

In this paper, we discuss the use of the GenAI techniques for the design of complex and innovative antennas, and demonstrate the potential of such techniques through the design and optimization of a dual-band choke ring antennas for millimeter-wave TT&C applications, complementing previously reported results on the topic [19, 20]. The details on the design method employed and, in particular, the use of a Variational Autoencoder (VAE) for the generation of a new choke-ring profile are first discussed. The electromagnetic simulation results of the final model generated by the VAE are also presented. Then, a thorough experimental verification of a fully-representative prototype is reported, demonstrating good agreement between simulation and measurement results. Finally, conclusions are drawn on the potential of GenAI for the development of complex antenna systems, together with perspectives on future works.

2. GenAI Design Method and Results

2.1. Antenna System Requirements

TT&C antennas are designed to provide hemispherical coverage through the generation of very wide radiation beams. To maintain a reliable communication link independently of the satellite attitude or orbital position, two antennas are generally installed on opposite spacecraft faces and combined through a hybrid coupler architecture [21]. Future LEO satellite communication constellations are considering Ka-band for these mission-critical TT&C links in order to leverage partial hardware sharing with

the payload subsystem and simplify the overall satellite RF architecture. An additional area of interest lies in integrating the separated transmit and receive frequency bands within a single antenna structure, despite a typical separation with a ratio of about 1:1.5. In this study, the Tx band is set to 19.7–20.2 GHz, whereas the Rx band is set to 29.5–30 GHz. The main design objective is to maximize the achievable beamwidth, defined as the angular range with a positive realized gain, while minimizing cross-polarization mismatch over said angular range.

The benchmark design for this work is the dual-band choke-ring antenna in [15]. That design uses a ridged-waveguide as the central feeding source for cross-sectional reduction and therefore a less directive pattern as a starting point, of particular importance in the upper frequency band. It was optimized using TICRA's CHAMP 3D tool [22], based on an efficient and accurate Body of Revolution Method of Moments (BoR-MoM), and available standard optimization techniques in TICRA's software. The benchmark design has 9 concentric chokes, leading to a profile with 37 points as illustrated in Fig. 1. With a conventional choke ring design, some of the variables are dependent (e.g., $x_1 = x_2$, $y_2 = y_3$, etc.) and the metallic wall between adjacent chokes is set to a minimum thickness by mechanical constraints (here, 1 mm), resulting in 18 independent variables. The optimized design achieved a directivity greater than 0 dBi up to ±75° in both Tx and Rx, and a cross-polarization discrimination (XPD) of more than 9.5 dB and 4.5 dB in each band, respectively. The primary goal of this work is thus to extend the minimum angular range for which the directivity exceeds 0 dBi, while preserving an XPD as high as possible across the corresponding field of view.

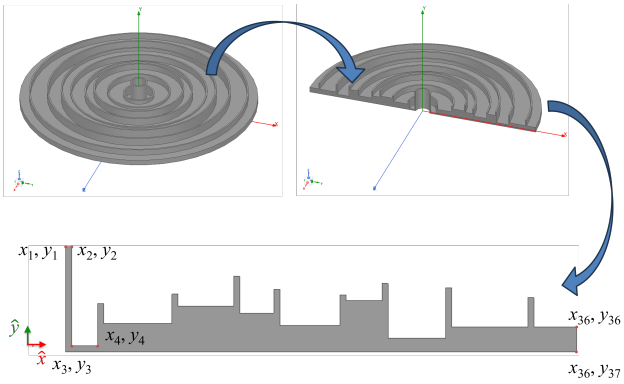


Figure 1: Perspective view, cross-sectional cut view and parametric description of the radial profile of an arbitrary choke-ring antenna design.

2.2. Data Generation and Transformation

To create the data set, each data point was generated by randomizing the parameters of an existing reference choke ring antenna, followed by evaluation through EM simulation using Ansys HFSS. Ultimately 500 randomized designs and their corresponding EM results were used to train the neural networks. To allow for more innovative profiles, the dependence between some of the variables discussed above was removed, and only the minimal wall thickness was maintained to ensure the manufacturability of the obtained designs.

Due to radial symmetry, the choke ring antenna design is effectively represented as a 2D cross sectional slice, or profile. This cross section is fully parameterized using a series of (x, y) coordinates to describe the 'edges' of the design, which are then simplified into rectangles of width and height. This final transformation imposes straight lines and right angles and allows the design to be fully parameterized in pairs of width, w, and height, h, measurements, with one pair per rectangle. In this instance, designs with 37 rectangles were considered, being equivalent to a design with 9 choke-rings but with more complex profiles, as shown in Fig. 2. This allows to reduce drastically the amount of information per data point, making the overall computational process more efficient.

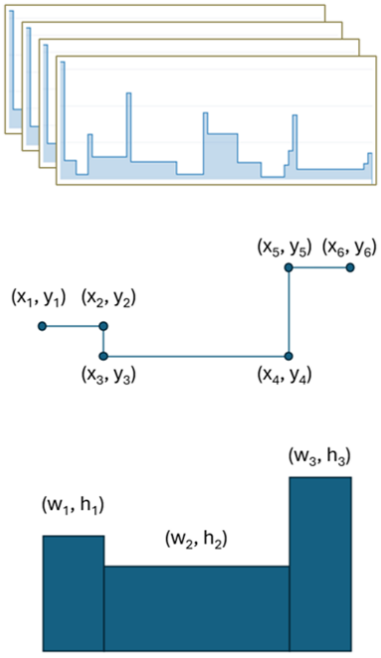


Figure 2: Data representation transformation from (x, y) coordinates to (w, h) rectangle coordinates.

The influence of the open-ended waveguide radius was investigated through statistical analysis of the generated dataset. The results, summarized in Fig. 3, clearly indicate that reducing the waveguide radius improves the achievable angular range over which the antenna gain remains acceptable, as also mentioned in connection with the benchmark design in Section 2.1. However, this improvement is accompanied here by a degradation in XPD. In addition, smaller waveguide radii exhibit a larger dispersion in performance, primarily due to the increased ripple levels observed in the radiation patterns.

Such reduced waveguide dimensions also necessitate the incorporation of a dielectric insert, or alternatively the use of ridged waveguide topologies, in order to ensure operation within the Tx frequency band, since the corresponding waveguide dimensions fall below the cut-off frequency. In the present work, ridged-waveguide solutions were intentionally avoided because they significantly complicate the transition design between the antenna and the feeding network. Finally, it should be noted that,

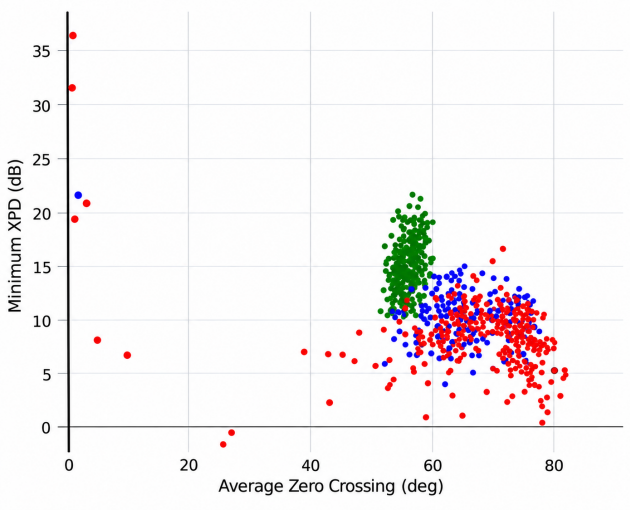


Figure 3: Statistical distribution of the training data key performance indicators generated in Rx with an open-ended waveguide radius of 5.4 mm (green), 3.8 mm (blue) and 3 mm (red).

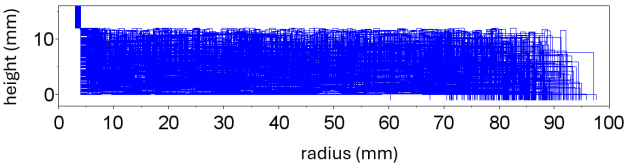


Figure 4: Overlapped choke ring antenna profiles of the training dataset.

due to project time constraints, the number of EM simulations and optimization iterations performed for dielectric-loaded configurations — and consequently included in the training dataset — remained limited.

The choke-ring antenna profiles generated for the training dataset are superimposed in Fig. 4, illustrating that the 500 design samples considered in this work provide a representative coverage of the accessible design space. The maximum choke height was limited to 12 mm, based on conclusions drawn from previous design studies [15].

The feeding structure, implemented as a dielectric-loaded open-ended waveguide, was kept identical across all dataset configurations in order to isolate the impact of the choke-ring geometry itself. The waveguide radius was fixed at 3 mm, while its height was allowed to vary between 12 and 16 mm. This arrangement ensures that the feeder section consistently extends above the choke-ring structure, a configuration that was observed to promote wider radiation beam patterns and improved hemispherical coverage characteristics.

2.3. Trade-off of GenAI Methods

Multiple GenAI models were considered for antenna design. The objective was to build a model that would generate designs with increased angular range ($> 70°$), while maintaining a minimum cross-polar discrimination (XPD) of at least 5 dB. We considered conditional Generative Adversarial Networks (cGANs), Transformers, and Variational Autoencoders (VAEs) for this activity.

GANs require relatively little data and are effective for generating novel antenna designs, as demonstrated in similar contexts [23]. However, they are prone to mode collapse [9], which limits output diversity. Test cGANs that were trained on the data available suffered from this due to the high non-linearity of the electromagnetic characterization of the choke-ring antenna and the relatively low amount of data. Although similarly complex problems have been solved with deep neural networks [24], these were using architectures that required significantly more data. However, this does not discount the possibility of investigating cGANs in the future.

Transformers are well suited for modeling sequential relationships in data [9]. Given the sequential nature of the design parameterization, it appears to be a natural fit, potentially allowing for the capture of higher level relationships between the antenna rings. A proof of concept model demonstrated that a transformer is able to learn a high-level representation of a simplified dataset. However, training the transformer on the antenna dataset was less successful and was not able to capture sufficient detail, although some learning was demonstrated. The Transformer's performance is impacted by data limitations, and larger datasets would be necessary to fully leverage their capabilities. Additionally, transformers typically operate on discrete data, making application to continuous-valued parameters less straightforward.

VAEs operate effectively on unlabeled data and provide robust data reconstruction on smaller datasets [25], such as the one used in this project. A trained VAE encodes a lower dimensional latent space representation of the dataset which can be sampled for new designs. While they are less suited to generating novel designs directly, this limitation can be addressed using a heuristic optimization process [26]. VAEs also mitigate the risk of creating physically invalid designs by creating a latent space based entirely on valid designs.

To support the trade-off, the three candidate models were trained under an identical protocol (494 designs, an 80/20 train–validation split, 100 epochs) and compared on validation reconstruction error and on an output-diversity ratio. The latter measures how much the generated profiles vary from one design to another: for each point along the profile, the standard deviation of its coordinate across the set of designs is computed, and these per-point standard deviations are averaged into a single spread value. The diversity ratio is this spread for the generated profiles divided by the same quantity measured on the ground-truth profiles, so a value of 1.0 matches the variability of the data while a value near 0 indicates that every output has collapsed to the same averaged profile. The numerical results obtained are compared in Fig. 5. The VAE reconstructed the profiles faithfully, with a validation error of 1.9 mm, a diversity ratio of 0.88 and all 16 latent dimensions active. The Transformer failed to reconstruct the profiles: its L1 loss plateaued at $\approx$3.3 by epoch 100 with a negligible train–validation gap, and its decoded outputs collapsed to a nearly identical averaged profile, giving a validation error of 10.1 mm and a diversity ratio of only 0.15. The cGAN did not converge to physically consistent geometries under the limited dataset and training

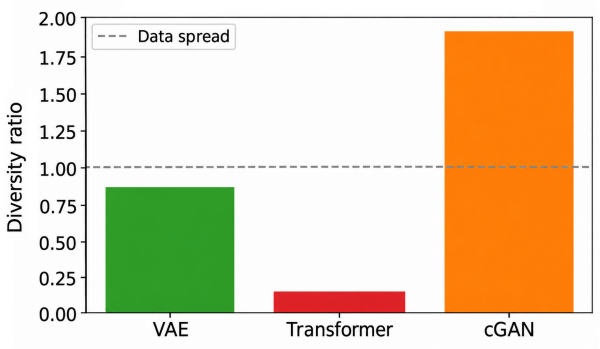


Figure 5: Profile diversity ratio (0 = mode collapse) of the compared GenAI methods under a common training protocol.

budget, producing unstructured, high-variance outputs rather than valid profiles. The cGAN and Transformer were therefore not pursued for generation.

2.4. Variational Autoencoder Application

A VAE specifically tailored for antenna design reconstruction was developed with the aim of effectively modeling the corresponding latent space. Various architectural configurations, hyperparameter settings, and loss functions were explored to optimize reconstruction fidelity. The selected architecture is schematically represented in Fig. 6.

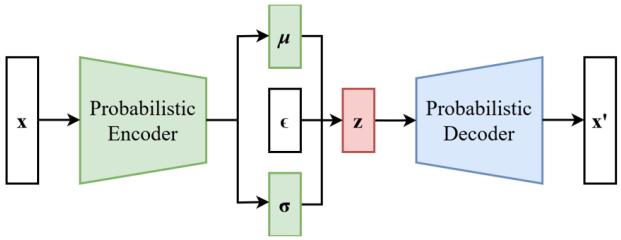


Figure 6: VAE model architecture.

2.4.1. Variational Autoencoder Architecture

The final VAE architecture is a stack of four 1-D convolutional layers (128 channels, batch normalization, LeakyReLU) that compress the profile into a 16-dimensional latent space, and a mirrored transposed-convolutional decoder reconstructs it. It was trained with the Adam optimizer (learning rate 5×10^{-3}, batch size 24) for 100 epochs. Here, the latent space is a compact, lower-dimensional set of continuous variables encoding each design, so that similar geometries map to nearby points; LeakyReLU is a non-linear activation passing positive values unchanged while allowing a small response to negative ones; and Adam is a widely used adaptive gradient-based training algorithm. The latent sample is drawn using the reparameterization

$$z = \mu + \varepsilon \odot \sigma \tag{1}$$

where μ and $\log\sigma^2$ are the encoder's predicted mean and log-variance of the latent vector z, $\varepsilon \sim \mathcal{N}(0,I)$ is a random noise vector and $\odot$ denotes the element-wise product. $\hat{x}$ is the decoder's reconstruction of the input profile x, and $\mathscr{L}_{KL}$ is the Kullback-Leibler (KL) divergence of the approximate posterior $\mathcal{N}(0,I)$ from the standard-normal prior $\mathcal{N}(0,I)$.

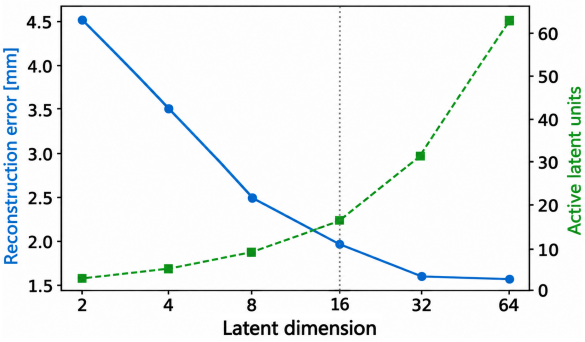


Figure 7: VAE latent-dimension selection.

The network is trained to minimize the combined loss

$$\mathscr{L} = \mathscr{L}_{recon} + \beta\mathscr{L}_{KL} \tag{2}$$

where

$$\begin{cases} \mathscr{L}_{recon} = \sum_i |x_i - \hat{x}_i| \\ \mathscr{L}_{KL} = -\frac{1}{2}\sum_{j=1}^{d}(1+\log\sigma_j^2 - \mu_j^2 - \sigma_j^2) \end{cases} \tag{3}$$

with an L1 reconstruction term, latent dimensionality $d = 16$ and a fixed weighting $\beta = 0.01$.

2.4.2. Training Details

Training used an 80/20 train–validation split (396/98 designs). The loss, reconstruction error and KL divergence converged within ∼20–40 epochs with no significant train–validation gap (limited overfitting), and all 16 latent dimensions remained active throughout (no posterior or latent-space collapse); the best-validation checkpoint (epoch 93) was retained.

The final architecture was selected under this common protocol by minimizing the validation reconstruction error (radial-profile L1 error, in mm) while monitoring the number of active latent units. Encoder width (32–256 channels) and depth (three to five convolutional layers) changed the validation error by less than 0.3 mm, with no benefit from the larger models, so the compact 128-channel, four-layer configuration was retained.

As shown in Fig. 7, the reconstruction error decreased monotonically with latent dimensionality (from 4.5 mm at $d = 2$ to 1.5 mm at $d = 64$) while every latent dimension remained active; $d = 16$ (1.9 mm) was chosen as the smallest latent space that preserved reconstruction fidelity while keeping the bottleneck compact for the subsequent latent-space search. The latent space remained fully active (all 16 dimensions) across a broad range of KL weights up to $\beta = 5$, so β was fixed at the small value 0.01 to prioritize reconstruction fidelity, with collapse of latent dimensions appearing only at much larger weights.

2.4.3. Latent Space Heuristic

Following model training, designs were systematically filtered within the latent space to exclude designs with undesirable performance characteristics. Specifically, antenna profiles were

removed if their XPD was less than 5 dB, or if their angular range in Tx was below 70°. This ensured that only good candidate designs were used for further analysis and optimization: of the ∼500 encoded designs, 17 met this performance threshold.

Within the feasible region of the latent space, a least-squares linear model was fitted from the latent coordinates of the feasible designs to their Tx angular range (transmission was deemed more important than reception); its unit-normalized coefficient vector defines the direction of steepest increase. This direction only sets where to move, not how far, so its scale was calibrated empirically to determine a suitable step size: each feasible design's latent coordinate was projected onto the unit direction (a scalar obtained as their dot product), and the ratio between the change in this projected coordinate and the corresponding change in Tx angular range was averaged over all pairs of feasible designs, yielding the latent-space distance equivalent to a 1° increase. The three best feasible designs were each perturbed along the direction using this calibrated step, in 21 increments from 0° to +20° of predicted gain, and decoded, producing 63 candidate profiles. Gain and XPD were obtained by full-wave EM simulation for every one of the 63 generated candidates; candidates had to satisfy XPD $\geq$ 5 dB in both bands, and among those the design maximizing Tx angular range was selected. This process yielded modest improvements in the angular range of the resulting designs, as shown in Fig. 8.

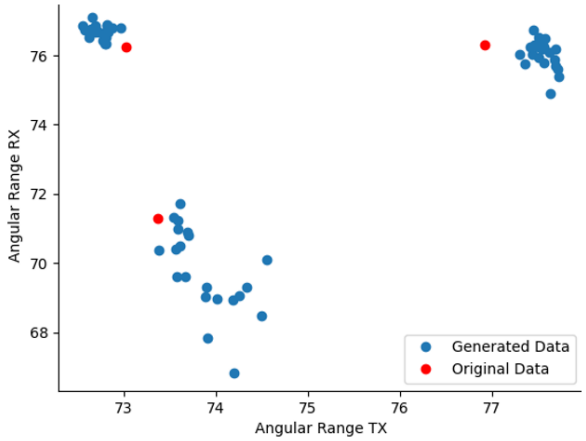


Figure 8: Comparison of angular range for original vs generated antenna designs.

2.5. Results

The best-performing antenna profile obtained after a reasonable number of optimization iterations is presented in Fig. 9. The proposed approach leads to a profile that deviates notably from conventional choke-ring designs, highlighting the potential of GenAI to explore novel solutions. Figures 10 and 11 show the simulated radiation patterns (co-polarization and XPD patterns) of the final choke-ring antenna model in Tx and Rx, respectively. This design achieved a directivity exceeding 0 dBi up to angular ranges of 77.5° and 75° in Tx and Rx, respectively. In addition, the worst-case XPD within the corresponding angular coverage remained above 5.5 dB in Tx and 5 dB in Rx.

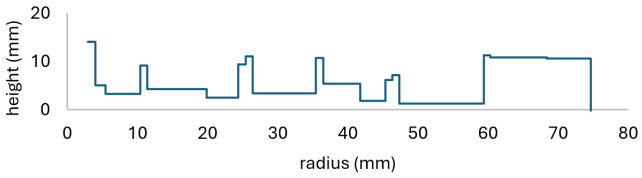


Figure 9: Best performing choke-ring profile generated using the trained VAE.

The proposed method does not replace full-wave EM analysis — the dominant cost — but reduces the number of geometries reaching the solver. Building the latent space exclusively from feasible designs prevents wasted simulations on invalid geometries, and optimization reduces to a low-dimensional search along a single direction, requiring only 63 full-wave EM simulations to exceed the conventionally optimized benchmark [15] in Tx angular range (77° vs 75°). A conventional global optimizer operating on the full geometric parameter set must both enforce validity and explore a higher-dimensional space, typically at a substantially higher simulation cost.

Although the observed improvements were small, they are significant as they validate the approach of using VAEs in this context. Future improvements could be achieved in two key ways. First, the newly generated antenna profiles may be incorporated into the original dataset, allowing for iterative continuous improvement in design performance. Second, expanding the underlying dataset to include a greater diversity of antenna designs would enable development of a more robust latent representation, potentially leading to improved results when repeating the optimization process.

3. Prototyping and Experimental Results

3.1. Prototyping

This section presents the prototyping of the AI-optimized choke-ring antenna design. The CAD model of the manufactured prototype is illustrated in Fig. 12, with perspective front and rear views. The antenna assembly is composed of two main sub-components: the radiating structure, implemented as a dielectric-loaded choke-ring antenna, and the feeding network, realized using a dual-band circular-waveguide septum polarizer interfaced through coaxial connectors.

The integration of the dielectric-to-hollow circular waveguide transition as well as the septum polarizer had some influence on the overall antenna performance, particularly with respect to XPD. In practice, interactions between the feeding network and the radiating structure can alter the electromagnetic field distribution and partially degrade the polarization purity. Consequently, future design iterations should incorporate the feeding element directly within the optimization and training process in order to achieve further improvements in the antenna performance and overall system integration.

Figure 13 presents the fabricated antenna prototype mounted on the mast of an MVG spherical near-field StarLab measurement facility. The antenna structure, including both metallic components and the dielectric insert, was manufactured using conventional CNC milling techniques. The overall antenna

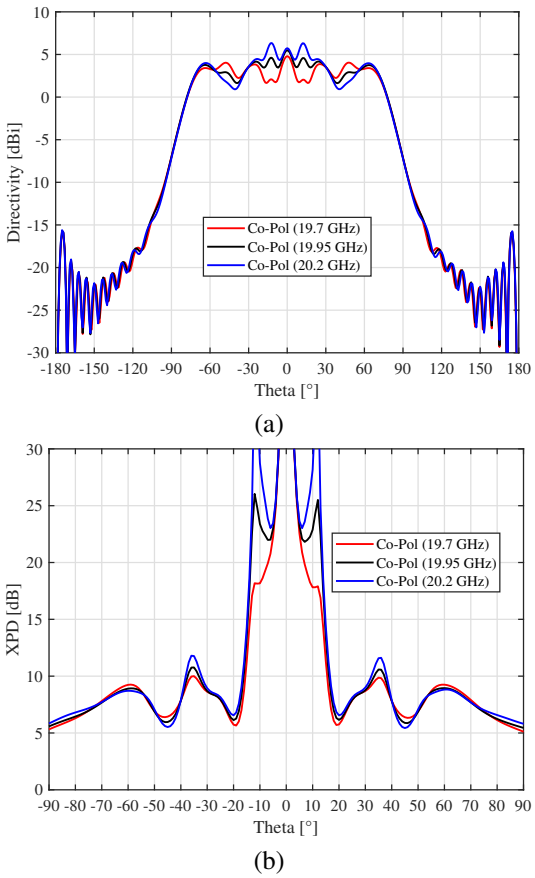


Figure 10: Simulated radiation performance of the final choke-ring antenna model in Tx: (a) co-polarization directivity patterns and b) XPD patterns (with ideal CP excitation at the input of the feeding waveguide).

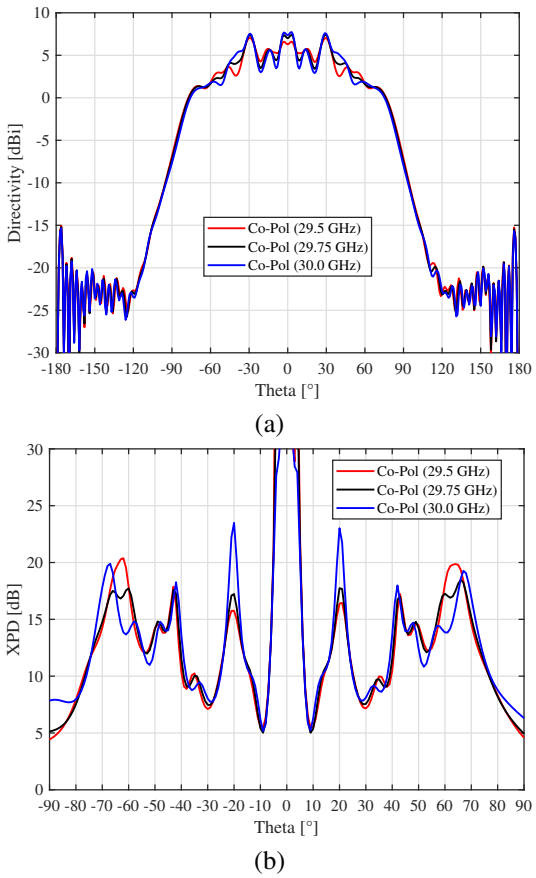


Figure 11: Simulated radiation performance of the final choke-ring antenna model in Rx: (a) co-polarization directivity patterns and b) XPD patterns (with ideal CP excitation at the input of the feeding waveguide).

dimensions are 154 × 154 × 66 mm³, with a total mass of approximately 220 g.

3.2. Experimental Results

The measurement uncertainty associated with the facility corresponds to a worst-case peak-gain uncertainty of approximately ±0.9 dB over the operational frequency range. This uncertainty may influence the evaluation of the considered performance metrics, particularly the determination of the angular region over which the antenna gain remains above 0 dBi. In contrast, the XPD, being a relative metric, is expected to be less sensitive to these measurement uncertainties.

Figures 14 and 15 compare the simulated and measured S-parameters of the antenna prototype across the Tx (port 1) and Rx (port 2) frequency bands, respectively. Overall, a good agreement is observed between simulation and measurement results, thereby validating both the antenna design methodology and the manufacturing approach.

The measured reflection coefficients (S11 and S22) exhibit a slight frequency shift on the order of 200-300 MHz relative to the simulated values. At the Tx center frequency of 19.95 GHz, the measured S11 and S21 parameters remain below -10 and -25 dB, respectively. Similarly, at the Rx center frequency of 29.75 GHz, both the measured S11 and S21 parameters remain below -20 dB, confirming adequate impedance matching and isolation performance across the operating bands. This frequency shift has been evaluated by retro-simulations as shown in Fig. 16. The principal contribution lies in the slight uncertainty on the dielectric insert positioning onto the open-ended waveguide feeder. Changing that position by about 100 µm yields the reported results that are in good agreement with the measurements. The manufacturing tolerances are the second factor for the observed discrepancies which, according to the retro-simulations, have been evaluated around ∼10 µm, as specified to the manufacturer. Despite these deviations, the measured RF performance remains satisfactory.

The simulated and measured radiation patterns of the antenna prototype are compared in Fig. 17, while the corresponding XPD results are presented in Fig. 18. The measurement campaign was conducted by sampling the radiation patterns over a range of 0° to 165° in ϕ with a step size of 15°, and from -180° to 180° in θ with a resolution of 2°, where ϕ and θ denote the conventional spherical coordinate angles.

At the Tx center frequency of 19.95 GHz, the fabricated antenna prototype achieves a realized gain exceeding 0 dBi up to an angular range of 75°, while maintaining an XPD greater than 2 dB over the corresponding coverage region. At the Rx center frequency of 29.75 GHz, the antenna exhibits a realized

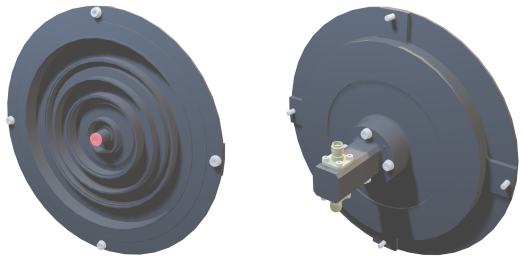


Figure 12: CAD model of the prototyped choke-ring antenna: perspective front-view (left) and perspective rear-view (right).



Figure 13: The choke ring antenna prototype in MVG's Starlab spherical near-field facility.

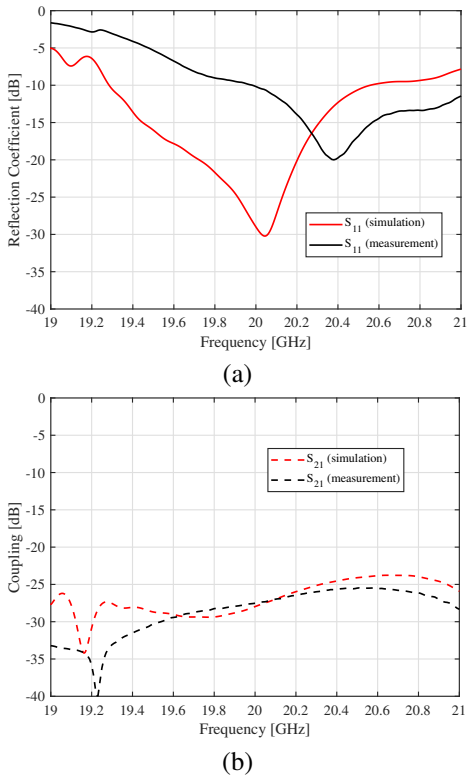


Figure 14: Simulated and measured (a) reflection coefficient and (b) port-to-port coupling in Tx.

gain above 0 dBi up to 73°, with an XPD greater than 4 dB.

The degradation in XPD observed in the Tx band is attributed to the presence of the dielectric to hollow waveguide transition as well as the septum polarizer. More specifically, the dielectric loading introduces additional reflections inside the feeder, which are subsequently re-radiated as undesired cross-polarized components. Given the fact that the scope of this research relates to the optimization process of the choke-ring part by means of GenAI, further investigations and design refinements are required to reduce the effect of the feeding mechanism and improve the polarization purity of the antenna.

Nevertheless, despite these limitations, a good overall agreement is observed between the simulated and measured results, thereby validating the proposed design methodology and the effectiveness of the AI-assisted optimization approach.

4. Conclusion

This paper investigated the application of artificial intelligence techniques to the design and optimization of dual-band choke-ring antennas. The aperture-level analyses demonstrated that the proposed AI-driven methodology is capable of achieving measurable performance improvements with respect to angular coverage and radiation characteristics. However, the subsequent integration of the feeding structure during prototype realization revealed a stronger impact on the overall antenna performance than initially anticipated, particularly in terms of polarization purity. Despite these effects, the experimental measurements remained in good agreement with the simulated predictions, thereby validating the overall design approach.

Several paths for future improvement have been identified. First, the newly generated antenna geometries obtained through the optimization process could be progressively incorporated into the original training dataset, enabling an iterative refinement strategy and continuous enhancement of the design performance. Second, enriching the dataset with a broader diversity of antenna topologies and geometrical configurations would allow the construction of a more representative and expressive latent space, potentially improving the effectiveness of subsequent optimization cycles.

More broadly, GenAI is expected to play a major role in the digital transformation of future SatCom system design. Its capability to rapidly explore high-dimensional design spaces, identify non-intuitive electromagnetic solutions, and adapt efficiently to evolving system constraints makes it a promising enabling technology for next-generation satellite and ground-segment architectures. Within the antennas and propagation community, this evolution may constitute a paradigm shift, moving from conventional manually guided and simulation-intensive optimization workflows toward AI-assisted design exploration and automated discovery. In this context, the work presented in this paper represents a promising first step toward the integration of GenAI methodologies into advanced antenna engineering processes.

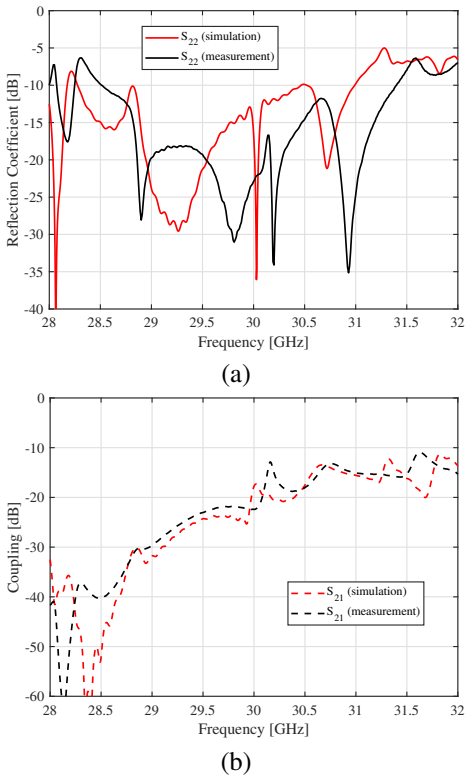


Figure 15: Simulated and measured (a) reflection coefficient and (b) port-to-port coupling in Rx.

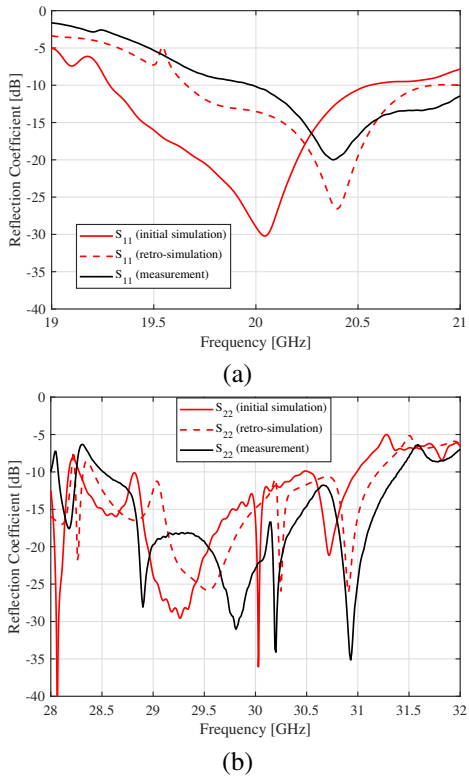


Figure 16: Retro-simulated vs measured reflection coefficient in (a) Tx and (b) Rx.

Acknowledgment

This activity was supported by the European Space Agency in the frame of an Advanced Research in Telecommunications Systems (ARTES) Future Preparation contract no. 4000144631.

References

[1] W. Hong *et al.*, "The role of millimeter-wave technologies in 5G/6G wireless communications," *IEEE J. Microwaves*, vol. 1, no. 1, pp. 101-122, Jan. 2021.

[2] Y. J. Guo, M. Ansari and N. J. G. Fonseca, "Circuit type multiple beamforming networks for antenna arrays in 5G and 6G terrestrial and non-terrestrial networks," *IEEE J. Microwaves*, vol. 1, no. 3, pp. 704-722, Jul. 2021.

[3] Y. J. Guo, M. Ansari, R. W. Ziolkowski and N. J. G. Fonseca, "Quasioptical multi-beam antenna technologies for B5G and 6G mmWave and THz networks: A review," *IEEE Open J. Antennas Propag.*, vol. 2, pp. 807-830, 2021.

[4] F. Zardi, P. Nayeri, P. Rocca and R. Haupt, "Artificial Intelligence for Adaptive and Reconfigurable Antenna Arrays: A Review," *IEEE Antennas Propag.* Mag., vol. 63, no. 3, pp. 28-38, Jun. 2021.

[5] S. K. Goudos, P. D. Diamantoulakis, M. A. Matin, P. Sarigiannidis, S. Wan and G. K. Karagiannidis, "Design of Antennas through Artificial Intelligence: State of the Art and Challenges," *IEEE Commun. Mag.*, vol. 60, no. 12, pp. 96-102, Dec. 2022.

[6] A. Gupta, E. A. Karahan, C. Bhat, K. Sengupta and U. K. Khankhoje, "Tandem Neural Network Based Design of Multiband Antennas," *IEEE Trans. Antennas Propag.*, vol. 71, no. 8, pp. 6308-6317, Aug. 2023.

[7] F. Peng and X. Chen, "An Antenna Optimization Framework Based on Deep Reinforcement Learning," *IEEE Trans. Antennas Propag.*, vol. 72, no. 10, pp. 7594-7605, Oct. 2024.

[8] https://oecd.ai/en/principles

[9] D. Foster, Generative deep learning: teaching machines to paint, write, compose, and play, First edition. Sebastopol, CA: O'Reilly Media, Inc, 2019.

[10] N. Capet, N. J. G. Fonseca and M. Romier, "Innovative antenna solution for NewSpace: Addressing the challenges of small satellite constellations," *Proc. Eur. Conf. Antennas Propag. (EuCAP)*, Stockholm, Sweden, Apr. 2025.

[11] E. Arnaud *et al.*, "Compact isoflux X-band payload telemetry antenna with simultaneous dual circular polarization for LEO satellite applications," *IEEE Antennas Wirel. Propag. Lett.*, vol. 19, no. 10, pp. 1679-1683, Oct. 2020.

[12] R. Ravanelli, C. Iannicelli, N. Baldecchi and F. Franchini, "Multiobjective optimization of an isoflux antenna for LEO satellite downhandling link," in *Proc. 18th Int. Conf. Microw., Radar Wireless Commun.*, Jun. 2010, pp. 1-4.

[13] M. Kilian, C. Hartwanger, A. Schinagl-Weiß and M. Schneider, "Xband downlink antenna characterised by

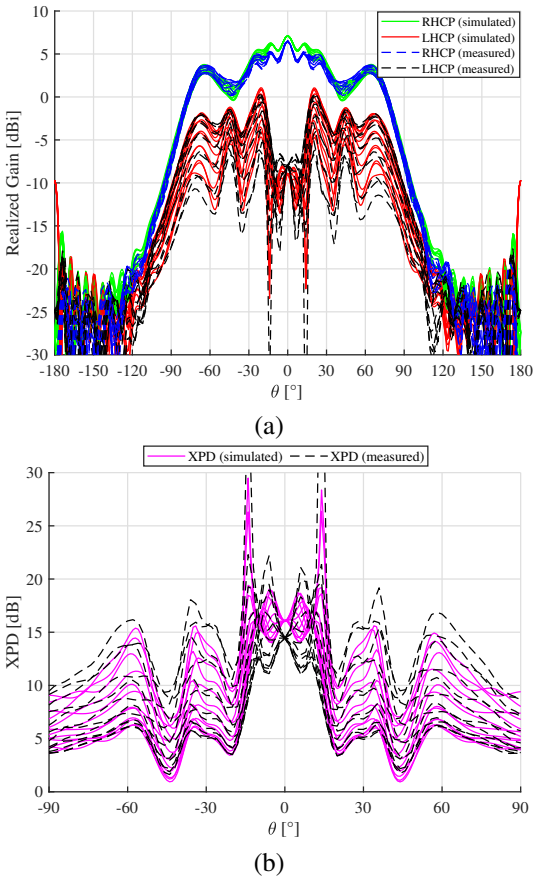


Figure 17: Simulated and measured radiation performance of the choke ring antenna prototype at 19.95 GHz: (a) co- and cross-polarization realized gain radiation patterns and (b) XPD patterns (including the feeding section).

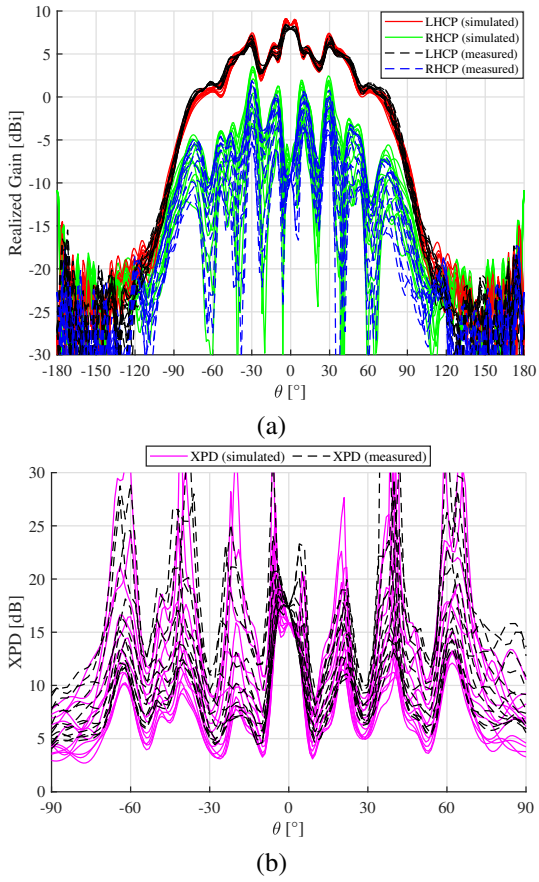


Figure 18: Simulated and measured radiation performance of the choke ring antenna prototype at 29.75 GHz: (a) co- and cross-polarization realized gain radiation patterns and (b) XPD patterns (including the feeding section).

isoflux gain mask," in *Proc. 11th German Microw. Conf. (GeMiC)*, 2018, pp. 21–24.

[14] P. Brachat, "Sectoral pattern synthesis with primary feeds," *IEEE Trans. Antennas Propag.*, vol. 42, no. 4, pp. 484-491, Apr. 1994.

[15] C. Stoumpos *et al.*, "Design of a dual-band dual-polarized choke-ring horn antenna for TT&C applications in Ka-band," in *Proc. 19th Eur. Conf. Antennas Propag. (EuCAP)*, Stockholm, Sweden, 2025, pp. 1-5.

[16] C. Stoumpos, Q. Guirando, Q. Lamotte, N. J. G. Fonseca and N. Capet, "Single- and Dual-band Circularly-Polarized Choke-Ring TT&C Antenna Solutions in Ka-band," in *Proc. IEEE Int. Symp. Antennas Propag. INC/USNC-URSI Radio Sci. Meeting (AP-S/INC-USNCURSI)*, Detroit, USA, 2026, pp. 1-4.

[17] O. A. Peverini, M. Lumia, G. Addamo, G. Virone and N. J. G. Fonseca, "How 3D-printing is changing RF front-end design for space applications," *IEEE J. Microwaves*, vol. 3, no. 2, pp. 800-814, Apr. 2023.

[18] C. Stoumpos *et al.*, "Ka-band choke-ring horn TT&C antenna combining conventional milling and aluminum selective laser melting (SLM) manufacturing," in *Proc. 43rd ESA Antenna Workshop*, Noordwijk, The Netherlands, Oct. 2025.

[19] N. J. G. Fonseca *et al.*, "Design of Dual-Band Millimeter-Wave Choke Ring Antennas Using Artificial Intelligence," in *Proc. 20th Eur. Conf. Antennas Propag. (EuCAP)*, Dublin, Ireland, 2026, pp. 1-5.

[20] N. J. G. Fonseca *et al.*, "A Dual-Band Choke Ring TT&C Antenna Designed Using Generative AI," in *Proc. Int. Appl. Comput. Electromagn. Soc. Symp. (ACES)*, Thessaloniki, Greece, May. 2026, pp. 1–2.

[21] A. Modenini and B. Ripani, "A tutorial on the tracking, telemetry, and command (TT&C) for space missions," *IEEE Commun. Surv. Tutor.*, vol. 25, no. 3, pp. 1510-1542, 2023.

[22] https://www.ticra.com/software/champ3d/

[23] P. Naseri, G. Goussetis, N. J. G. Fonseca, and S. V. Hum, "Synthesis of multi-band reflective polarizing metasurfaces using a generative adversarial network," *Sci. Rep.*, vol. 12, no. 1, p. 17006, Oct. 2022.

[24] N. Thuerey, K. Weissenow, L. Prantl, and X. Hu, 'Deep Learning Methods for Reynolds-Averaged Navier-

Stokes Simulations of Airfoil Flows', 2018, doi: 10.48550/ARXIV.1810.08217.

[25] D. P. Kingma and M. Welling, 'Auto-Encoding Variational Bayes', Dec. 10, 2022, doi: 10.48550/arXiv.1312.6114.

[26] A. Tripp, E. Daxberger, and J. M. Hernández-Lobato, 'Sample-Efficient Optimization in the Latent Space of Deep Generative Models via Weighted Retraining', Oct. 25, 2020, doi: 10.48550/arXiv.2006.09191.